Ring waves as a mass transport mechanism in air-driven core-annular flows

Roberto Camassa,[1] M. Gregory Forest,[1] Long Lee,[2] H. Reed Ogrosky,[1] and Jeffrey Olander[1,3]
[1]*Carolina Center for Interdisciplinary Applied Mathematics, Department of Mathematics, University of North Carolina, Chapel Hill, North Carolina 27599-3250, USA*
[2]*Department of Mathematics, University of Wyoming, Laramie, Wyoming 82071-3036, USA*
[3]*Department of Physics, University of North Carolina, Chapel Hill, North Carolina 27599-3255, USA*

(Received 6 May 2011; published 11 December 2012)

Air-driven core-annular fluid flows occur in many situations, from lung airways to engineering applications. Here we study, experimentally and theoretically, flows where a viscous liquid film lining the inside of a tube is forced upwards against gravity by turbulent airflow up the center of the tube. We present results on the thickness and mean speed of the film and properties of the interfacial waves that develop from an instability of the air-liquid interface. We derive a long-wave asymptotic model and compare properties of its solutions with those of the experiments. Traveling wave solutions of this long-wave model exhibit evidence of different mass transport regimes: Past a certain threshold, sufficiently large-amplitude waves begin to trap cores of fluid which propagate upward at wave speeds. This theoretical result is then confirmed by a second set of experiments that show evidence of ring waves of annular fluid propagating over the underlying creeping flow. By tuning the parameters of the experiments, the strength of this phenomenon can be adjusted in a way that is predicted qualitatively by the model.

DOI: 10.1103/PhysRevE.86.066305 PACS number(s): 47.55.Iv, 87.85.gf

I. INTRODUCTION

Core-annular flows arise in many applications (e.g., oil recovery, lung pathways) where one fluid phase occupies the core and an immiscible, more viscous fluid occupies the annulus between the pipe wall and core. (Identical and lower viscosity annular phases are relevant to applications outside of our interest here; cf. Ref. [1].) Interfacial instabilities, their growth rates, and saturation in coherent or irregular structures, and the propagation of interfacial structures in driven core-annular flow have been extensively explored both experimentally and theoretically. Motivated by applications, these studies have focused primarily on viscosity contrasts typical of oil and water, low Reynolds numbers in both phases (creeping flows), thin annular layers relative to the tube radius, and small capillary numbers (surface tension forces dominate viscous forces) [1–17]. Our focus here is on the mechanisms by which forced steady airflow transports annular layers of high-viscosity fluids, conditions appropriate to (large) lung airways. Notable experimental work on this topic goes back to Clarke *et al.* [18] and to Kim *et al.* [19–21], where the added complexity of a viscoelastic fluid in the annular layer was also considered. In lung biomechanics it is held that airway surface liquids move toward the larynx as an annular creeping flow. Mechanisms driving the flow include the coordinated motion of carpets of cilia and air drag from tidal breathing or cough. The relative mass transport rates of these mechanisms are not known and are beyond the focus of this study.

In this work we duplicate the experiment of Kim *et al.* [20] on air drag transport of annular wetting layers, with special attention to the *mechanisms* of mass transport not addressed in Ref. [20]. One such mechanism certainly involves annular waves, which are spawned via interfacial instability or growth of perturbations at the annular fluid source. Simply by increasing the surface roughness of the liquid phase, it is to be expected that waves could enhance the exchange of momentum between core and annular fluids. In this article we show that, under certain conditions, these waves play a more direct role by trapping a propagating fluid core *between* the wetting annular layer and air. Each trapped core is a bolus of annular fluid that translates relative to the underlying creeping flow, thus providing a mass transport mechanism. For a traveling wave, viewed in the wave frame of reference, this would correspond to a region of closed streamlines. We hereafter refer to these waves as *mass transport waves*; conversely, we shall refer to waves without a trapped core as *shear waves* since these modify the shear flow only by fanning and constricting the corresponding *open* streamlines. Trapped cores in core-annular flow were previously identified theoretically in models of water-oil flows at low Reynolds numbers [2]. We show experimentally and theoretically that such structures likewise arise in turbulent air-driven annular

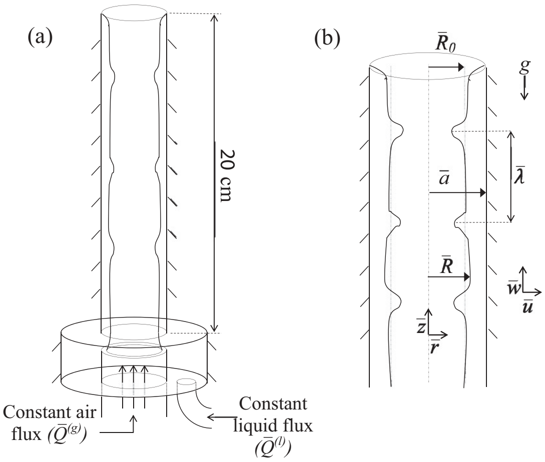

FIG. 1. (a) Schematic diagram of the experimental setup. Air is forced upward through the tube while high viscosity fluid is supplied through an annular slit. (b) Definition sketch of the flow variables.

©2012 American Physical Society

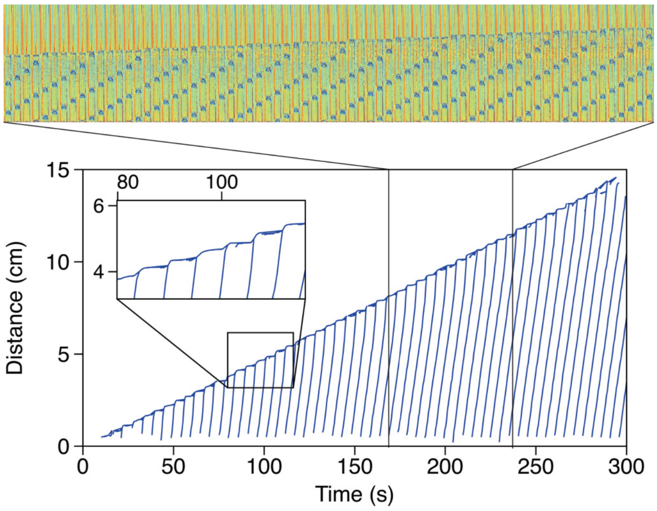

FIG. 2. (Color online) Color montage: successive snapshots of the tube. Plot: Tracked wave crests in the tube (liquid volume flux = 1.0 cm^3/min, gas volume flux = 330 cm^3/s, liquid viscosity = 600 P, snapshots 1 s apart). Each line represents one crest as it travels up the tube. Inset zooms in on the front advancement whenever a crest reaches the wetting front.

oil flow. These conditions are designed to mimic the trachea and upper lung airways, with oil as a high viscosity proxy for mucus. These ring waves are distinct from so-called plugs in lung airways, which divide and disconnect the air core under low Reynolds number airflow conditions [22].

The paper is organized as follows: In Sec. II we present the results of experiments similar to Ref. [20]. In Sec. III a long-wave asymptotic model is constructed and briefly compared to the thin-film model in Ref. [2]. In Sec. IV we find traveling wave solutions to the model and compare them with the experiments. Section V contains the results of further experiments which highlight the role of waves in transporting mass. We conclude with a brief discussion of the results in Sec. VI.

II. PRELIMINARY EXPERIMENTS

The experimental setup, after Ref. [19,20], is depicted in Fig. 1(a). A 20.0 cm glass tube with a 1.0 cm inner diameter represents the trachea. First, the tube is inserted into an O-ring-lined hole in the lid of an annular chamber made of stainless steel and glass. Next, liquid is forced into the annulus of the chamber at a constant volume flux by a Harvard Apparatus Model 975 Syringe Pump and is allowed to fill the chamber up to a small annular gap. The gap is adjustable, set to 1 mm for the experiments reported here. Finally a constant volume flux of air is forced through the core of the chamber by an Aalborg Digital Flow Controller where it meets the liquid at the gap. Over the course of the experiment, liquid is forced into the gap and dragged upward into the tube by sufficiently fast air flows. In a matter of minutes, the liquid wetting front advances to the top of the tube, completely coating the inner surface. When the liquid reaches the top, it spills over into a collection cup. We focus on the waves' contribution to the advancement of the wetting front as well as the long-time air-liquid interfacial dynamics.

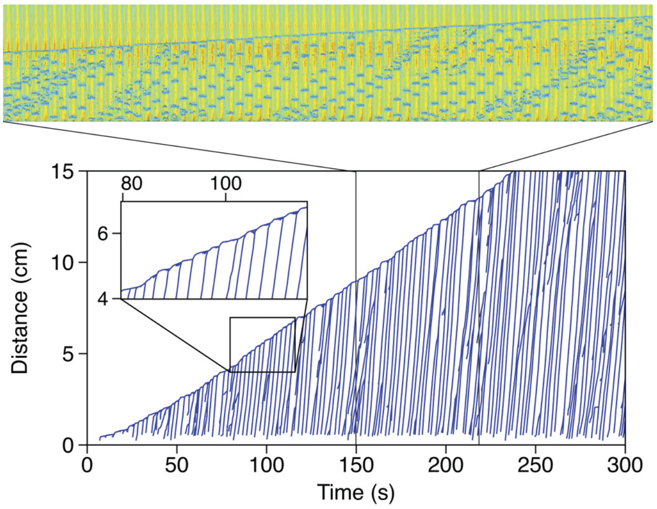

FIG. 3. (Color online) Same as Fig. 2 but with spatiotemporal chaotic behavior (liquid volume flux = 1.0 cm^3/min, gas volume flux = 670 cm^3/s, liquid viscosity = 129 P, snapshots 0.5 s apart).

We use two silicone oils with viscosities of 129 P and 600 P. Oil densities were calculated with an Anton Paar DMA 4500 density meter to be 0.95–0.98 g/cm^3. The liquids are injected into the apparatus with a constant volume flux in the range 0.5-1.0 cm^3/min, while air is forced through the apparatus at a constant volume flux in the range 330–1170 cm^3/s. As each experiment progresses, waves develop and travel from the bottom of the tube to the wetting front. These waves are tracked by HD video recording.

We then use a MATLAB script to track the waves and to find the statistics of various wave properties like speed and frequency. Figures 2 and 3 show montages of the tube video footage paired with the results of the tracking. At first glance one sees an evident front advancement phenomenon: The front advances in spurts precisely when a new wave arrives. This strongly suggests the hypothesis that *these are mass transport waves as opposed to shear waves.* Furthermore, since the core air stream is continuous, these putative mass waves are torus shaped, which we call ring waves by analogy with vortex rings.

The properties of the liquid film and the interfacial waves are worth discussing. Figure 4(a) shows the trend of mean thickness of the film as a function of air volume flux for various viscosities and oil fluxes. The film thickness decreases with increasing airflow rate, decreasing viscosity, and decreasing liquid flux. These results were found by letting the experiments run for several minutes after the entire tube was coated with oil. The liquid was then weighed using an Ohaus Adventurer high-precision scale. The film thickness was calculated using this weight, the oil density, and the tube inner radius. For each set of parameters several experiments were performed; both the average mean thickness and range of thicknesses are displayed. In Fig. 4(b) we plot the mean speed of the liquid film by dividing the liquid volume flux by the liquid's cross-sectional area calculated from the mean thickness. (Dashed lines correspond to results from the model derived in Sec. III; further discussion of these results is taken up in Sec. IV.)

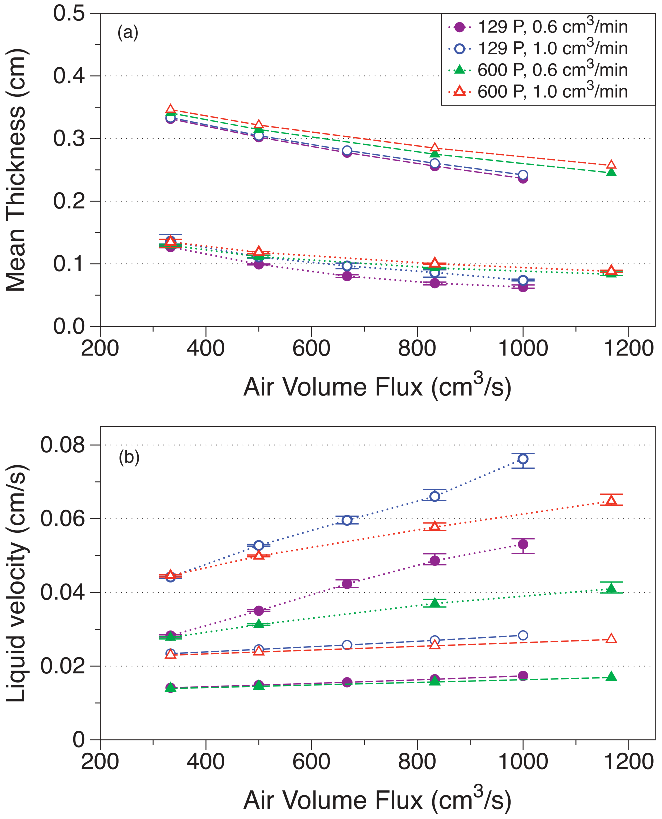

FIG. 4. (Color online) (a) Mean thickness of the liquid film for various viscosities $\mu^{(l)}$, liquid fluxes $Q^{(l)}$, and air fluxes $Q^{(g)}$. Bars indicate range of values over several trials of each experiment. Dotted lines indicate trends in experimental data; dashed lines represent model predictions (see Sec. IV for discussion). (b) Mean liquid cross-sectional average velocities calculated using data in panel (a).

Figure 5 shows the mean wave velocity, wavelength, and wave mass for experiments where $\mu^{(l)} = 129$ P and $Q^{(l)} = 1.0$ cm^3/min; error bars represent one standard deviation. The wave mass was calculated in the following way. From the steplike advancement of the wetting front upon the arrival of each wave, we determine the step height per wave crashing event. The mean thickness of the liquid film, the geometry of the tube, and the wetting front displacement then determine the approximate mass of liquid in each wave. Figures 6 and 7 present the distributions of wave velocities and wavelengths, respectively, used to construct Figs. 5(a) and 5(b).

Note that an increase in airflow rate, with liquid volume inflow rate held fixed, leads to slower, shorter wavelength, and less massive trapped cores. These observations suggest a threshold airflow rate at which the dominant mechanism of mass transport shifts from ring waves to the more widely held mode of creeping shear flow of the wetting layer. This shift is confirmed by the model and simulations given below. The creeping shear mode transport would more closely resemble the exact Navier-Stokes solution for the core-annular pipe flow problem, which is formed by nested Poiseuille flows with constant interfacial diameter. However, such an exact solution is far from the experimentally observed regimes; in particular, the mean (airflow) core diameter for the exact solution would be much smaller than that measured in the experiments, which implies that the actual stress applied by the air to the annular liquid layer is much larger in the experiment than in the exact Poiseuille regime.

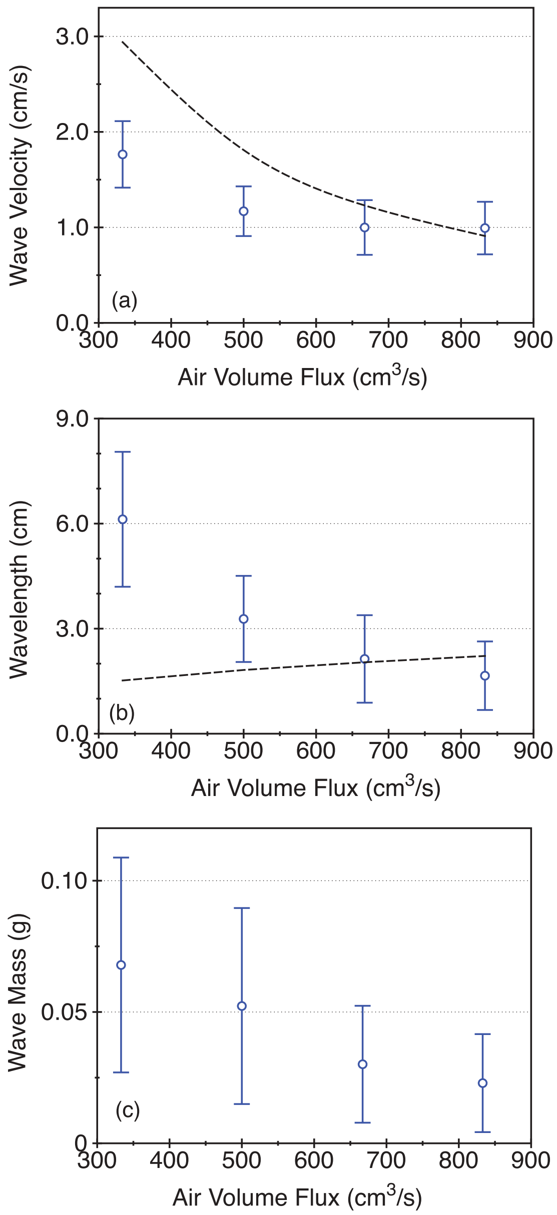

FIG. 5. (Color online) Mean values of wave (a) velocity, (b) wavelength, and (c) mass with bars indicating one standard deviation. Dashed lines represent model predictions (see Sec. III). $Q^{(l)} = 1.0$ cm^3/min, $\mu^{(l)} = 129$ P.

III. LONG-WAVE ASYMPTOTIC MODEL

We are interested in modeling axisymmetric disturbances in a two-phase vertical pressure-driven core-annular flow with the (much) more viscous fluid in the annulus, and we summarize the model developed in Ref. [23] with some extensions. As our primary motivation is flow with a gas core and liquid annulus, we refer to the core variables with the superscript (g) and

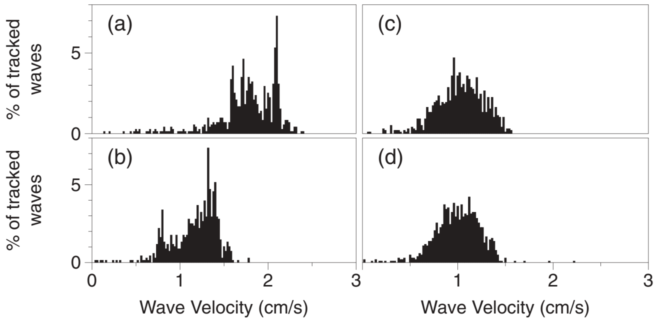

FIG. 6. Distribution of wave velocities in Fig. 5(a) for airflow rates of (a) 333 cm^3/s, (b) 500 cm^3/s, (c) 667 cm^3/s, (d) 833 cm^3/s.

the annular variables with the superscript (l) throughout. The governing equations for the flow of both the gas and the liquid are the incompressible axisymmetric Navier-Stokes equations in cylindrical coordinates:

$$\bar\rho(\bar u_{\bar t}+\bar u\bar u_{\bar r}+\bar w\bar u_{\bar z}) = -\bar p_{\bar r}+\bar\mu\left[\frac{1}{\bar r}\partial_{\bar r}(\bar r\bar u_{\bar r})+\bar u_{\bar z\bar z}-\frac{\bar u}{\bar r^2}\right],$$
$$\bar\rho(\bar w_{\bar t}+\bar u\bar w_{\bar r}+\bar w\bar w_{\bar z}) = -\bar p_{\bar z}+\bar\mu\left[\frac{1}{\bar r}\partial_{\bar r}(\bar r\bar w_{\bar r})+\bar w_{\bar z\bar z}\right]-\bar\rho\bar g,$$
$$\frac{1}{\bar r}\partial_{\bar r}(\bar r\bar u)+\bar w_{\bar z}=0, \tag{1}$$

where the coordinates are $(\bar r,\bar\theta,\bar z)$ with associated velocity components $(\bar u,\bar v,\bar w)$ [see Fig. 1(b)]. Here $\bar p$ is pressure, $\bar\rho$ is density, $\bar\mu$ is molecular viscosity, and $\bar g$ is gravity. All dimensional quantities are marked by overbars, and subscripts denote partial derivatives.

We nondimensionalize (1) with a typical (wave)length scale in the $\bar z$ direction, $\bar\lambda$, and a typical length scale in the $\bar r$ direction, $\bar R_0$, the radius of the cross section of the gas core. If $\epsilon = \bar R_0/\bar\lambda \ll 1$ the distortions to the air-liquid interface are long-wave. Other scales are set by the gas core centerline laminar axial velocity $\bar W_0 = 2\bar Q^{(g)}/(\pi\bar R_0^2)$ and a radial velocity $\bar U_0 = \epsilon\bar W_0$.

We then nondimensionalize (1) with the following variables:

$$r=\bar r/\bar R_0,\quad z=\bar z/\bar\lambda,\quad u=\bar u/\bar U_0,\quad w=\bar w/\bar W_0,$$
$$t=\bar t\bar W_0/\bar\lambda,\quad p=\epsilon\bar p\bar R_0/(\bar\mu^{(l)}\bar W_0),\quad \tau=\bar\tau\bar R_0/(\bar\mu^{(l)}\bar W_0), \tag{2}$$

where t is the dimensionless time, τ is the dimensionless tangential stress, and p is the dimensionless pressure. Important parameters in the problem are the Reynolds number $\mathrm{Re}^{(l)} \equiv \bar\rho^{(l)}\bar W_0\bar R_0/\bar\mu^{(l)}$ and Froude number $\mathrm{Fr} = \bar W_0/\sqrt{\bar g\bar R_0}$.

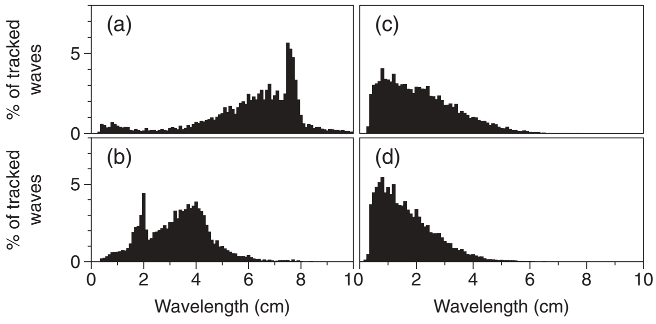

FIG. 7. Distribution of wavelengths in Fig. 5(b) for airflow rates of (a) 333 cm^3/s, (b) 500 cm^3/s, (c) 667 cm^3/s, (d) 833 cm^3/s.

We substitute (2) into (1) and take the limit $\epsilon \to 0$. For fixed mean radius $\bar R_0$, the liquid has fixed Reynolds number and hence $\epsilon\mathrm{Re}^{(l)} \to 0$. To leading order then (1) becomes

$$0 = p_r, \tag{3}$$

$$\frac{1}{r}\partial(rw_r) = p_z + \frac{\mathrm{Re}^{(l)}}{\mathrm{Fr}^2}, \tag{4}$$

$$\frac{1}{r}\partial_r(rw)+u_z = 0. \tag{5}$$

The boundary condition at the wall $r = a$ is

$$w = 0. \tag{6}$$

At the interface $r = R(z,t)$ we require continuity of tangential stress

$$w_r = \tau^{(g)} \tag{7}$$

and continuity of normal stress

$$-p^{(l)} = -p^{(g)} + \frac{\epsilon}{C}(R^{-1}-\epsilon^2 R_{zz}) \tag{8}$$

after long-wave asymptotics is used to estimate the curvature in the longitudinal direction, and where $C = \bar W_0\bar\mu^{(l)}/\bar\gamma$ is the capillary number. While the higher-order terms vanish as $\epsilon \to 0$ in Eq. (8), it is essential to retain the surface tension terms at the leading order, for which one term is of $O(\epsilon)$ and the other is of $O(\epsilon^3)$. The $O(\epsilon)$ term is responsible for instability growth from an initial disturbance while the $O(\epsilon^3)$ term stabilizes the instability growth. Hence it is important to retain both of them, regardless of the order of magnitude (see, e.g., Ref. [24] for a discussion).

The kinematic condition at the interface is

$$u = R_t + wR_z. \tag{9}$$

Integrating the continuity equation (5) across the annular-sectional area of the liquid and using (9) yields the layer-mean equation,

$$R_t - \frac{1}{R}\frac{\partial}{\partial z}\int_R^a wr\,dr = 0, \tag{10}$$

for the interface location; an approximate expression for w would then make (10) a decoupled equation for the evolution of the interface.

The boundary value problem (3), (4), and (6)–(8) can be solved for w in terms of the unknown quantities $p_z^{(g)}$ and $\tau^{(g)}$. The air flow in all our experiments is at a high enough Reynolds number ($\mathrm{Re}^{(g)} > 3000$) to be fully turbulent. Hence, to estimate these terms, we model the gas flow using the so-called zero equation turbulence closure [25]. A crude way to account for turbulent effects is to use an effective viscosity based on the Blasius formula [25] instead of the actual molecular viscosity,

$$\mu_{\mathrm{eff}}^{(g)} = 0.0791\frac{(\mathrm{Re}^{(g)})^{3/4}\mu^{(g)}}{16}, \tag{11}$$

where $\mathrm{Re}^{(g)} = \bar\rho^{(g)}\bar W_0\bar R_0/\bar\mu^{(g)}$. The mean gas flow uses a locally Poiseuille solution with this viscosity, and we modulate this to take into account the slow variation in z of the gas-liquid interface. Since $m = \bar{\mu}^{(l)}/\bar{\mu}^{(g)} = O(10^6)$, we assume that the velocity at the interface $r = R(z,t)$ is of order ϵ or smaller. Hence we take the mean velocity of the gas to be

$$w^{(g)}(r) = \frac{m}{4}\left(p_z^{(g)} + \frac{\bar{\rho}^{(g)}\mathrm{Re}^{(l)}}{\bar{\rho}^{(l)}\mathrm{Fr}^2}\right)(r^2 - R^2). \tag{12}$$

By integrating the velocity field across the core region, the two unknowns $p_z^{(g)}$ and $\tau^{(g)}$ can be estimated in terms of the fixed gas flux and interface location. Substituting $p_z^{(g)}$ and $\tau^{(g)}$ into the liquid velocity field w, and w into (10), gives the evolution equation for the interface:

$$\begin{aligned} R_t &+ [S_1 f_1(R;a) + S_2(a) f_2(R;a)]R_z \\ &+ \frac{S_3(a)}{R}[f_3(R;a)(R_z + R^2 R_{zzz})]_z = 0, \end{aligned} \tag{13}$$

where the f_i are given by

$$\begin{aligned} f_1(R;a) &= \frac{a^2}{R^4}\left(\frac{a^2}{R^2} - 1\right), \\ f_2(R;a) &= R^2 - a^2 + 2R^2 \ln\left(\frac{a}{R}\right), \\ f_3(R;a) &= \frac{a^4}{R^2} - 4a^2 + 3R^2 + 4R^2 \ln\left(\frac{a}{R}\right), \end{aligned} \tag{14}$$

and the S_i by

$$S_1 = \frac{1}{m}, \quad S_2(a) = \frac{(\bar{\rho}^{(l)} - \bar{\rho}^{(g)})\mathrm{Re}^{(l)}}{2\bar{\rho}^{(\ell)}\mathrm{Fr}^2}, \quad S_3(a) = \frac{1}{16C}. \tag{15}$$

The functional notation for S_2 and S_3 highlights their dependence on a. Note that (13) does not depend on either the thickness of the annulus being small or on the interfacial disturbances being weakly nonlinear; i.e., the model is fully nonlinear and still contains the cylindrical geometry of the original problem. If (13) is rescaled in time, the dynamics of the model can be completely determined by the value of three parameters: $F(a) = S_2/S_1$, $S(a) = S_3/S_1$, and a.

If the annular film is thin, Eq. (13) can be further simplified by letting

$$\eta = 1 - \frac{R}{a}; \tag{16}$$

$\eta \ll 1$ represents the thickness of the thin annular film. Each of the functions $f_i(R;a)$ in Eq. (14) can be expanded about $\eta = 0$:

$$f_1(\eta) = \left(\frac{2}{a^2}\right)\eta + \left(\frac{11}{a^2}\right)\eta^2 + \left(\frac{36}{a^2}\right)\eta^3 + O(\eta^4), \tag{17}$$

$$f_2(\eta) = (-2a^2)\eta^2 + \left(\frac{2a^2}{3}\right)\eta^3 + O(\eta^4), \tag{18}$$

$$f_3(\eta) = \left(\frac{16a^2}{3}\right)\eta^3 + O(\eta^4). \tag{19}$$

The gravity term f_2 vanishes at leading order; i.e., the effects of interfacial tangential stress dominate the effects of gravity in the thin-film limit. As before, $f_3 = O(\eta^3)$ is retained to keep the effects of surface tension. Substituting (16)–(19) into (13) gives

$$\eta_t + \frac{2}{ma^2}\eta\eta_z + \frac{a^3}{3C}[\eta^3(\eta_z + a^2\eta_{zzz})]_z = 0, \tag{20}$$

whose solutions have been studied in Refs. [2,26]. In Ref. [2] the radial coordinate is stretched across the annular fluid, so that the thickness of the fluid is $h = \frac{a}{\beta}\eta$ where $\beta = a - 1 \ll 1$. Applying this stretch to (20) and rescaling in time by the speed of the undisturbed interface gives (to leading order in β)

$$h_t + hh_z + S^*[h^3(h_z + h_{zzz})]_z = 0, \tag{21}$$

where

$$S^* = \frac{m}{6C}\beta^2 = \frac{\pi\bar{\gamma}\bar{R}_0^2}{12\bar{Q}^{(g)}\bar{\mu}^{(g)}}\beta^2. \tag{22}$$

Note that (21) is a conservation law for h, so that mass in a planar sense is conserved. This is in contrast to (13) which is a conservation law for R^2. (The consequences of this will be returned to briefly in Sec. IV, but a full discussion lies somewhat outside of the goals of this work and will be discussed elsewhere.)

IV. MODEL RESULTS

The experimental observations clearly show that traveling wave solutions play a central role in most experimental regimes. These solutions can then be analyzed to provide information on fluid transport independently of time evolution. Since our model is not exactly solvable, we employ an iterative numerical strategy. A good initial guess for this, as well as information on time dependent regimes, can be provided by solving the PDE (13) with the method of lines and a pseudospectral method (whereby the spatial derivatives are calculated in Fourier space and the nonlinearities are calculated in physical space). A second-order predictor-corrector scheme for time integration is used.

Throughout the scheme implementation, the Fourier modes of the derivatives and nonlinear terms are carefully monitored to ensure conservation of volume. The strongly nonlinear terms require dealiasing of the Fourier coefficients after each time step. To ensure that all suppressed modes are insignificant in the evolution, the spectra of R, R^{-1}, and $\log R$ are monitored, along with the mass of the liquid. If the suppressed modes become significant (or the total volume of liquid varies), spatial resolution is increased. For initial conditions, we perturb the interface with either a single mode or multiple modes (typically 6), i.e., $R(z,0) = R_0 - \sum_{k=1}^{6} b\cos(2\pi kz + \alpha_k)$ where α_k is a random phase shift for each mode and typically $b < 0.05(a - 1)$ for the amplitude.

As the interface evolves, instabilities grow due to the azimuthal curvature of the interface, which enters (13) through the term $f_3(R;a)R_z$. The axial curvature has a stabilizing effect for long waves through the term $f_3(R;a)R^2R_{zzz}$. The interface eventually develops into a series of waves that either exhibit spatiotemporal chaotic behavior or form a train of traveling waves or pulses; examples can be seen in Figs. 8 and 9. (See also Ref. [27] for a mathematical assessment of the stabilizing effects of higher derivative terms in PDE's with similar structure.)

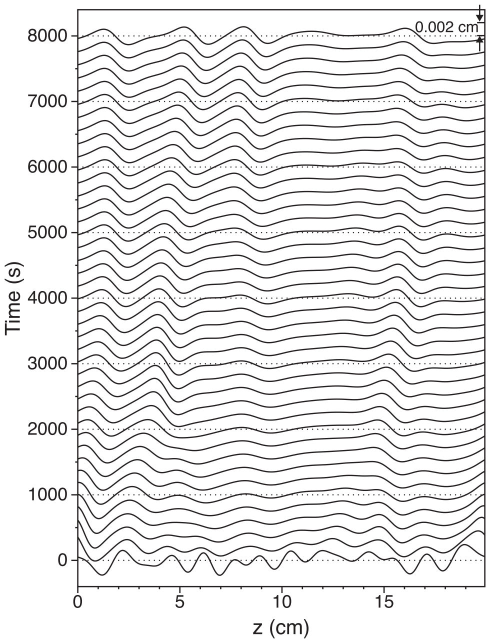

FIG. 8. Time snapshots showing the evolution of solutions to Eq. (13) in a periodic domain for $S \approx 0.051$, $F \approx 2.92$, and $a \approx 1.24$ [corresponding to experiment with $Q^{(l)} = 0.6$ cm^3/min, $Q^{(g)} = 667$ cm^3/s, $\mu^{(l)} = 129$ P, and modified effective viscosity given by (23)]. Interfacial profiles are shown successively shifted at time intervals $\Delta t = 200$ s. Profiles are shown in the frame of reference moving with an undisturbed interface. Dotted lines indicate mean thickness for the selected snapshots; amplitude scale is given on the right-hand side.

The model may be used to predict the thickness of the liquid film by monitoring the liquid flux as the interface evolves. The experiments in Sec. II were conducted with fixed liquid flux, but this flux condition is not automatically matched in our model simulations. By employing an iterative bisection-method strategy, the mean film thickness that produces a flux within the desired accuracy of the experimental value is found (to within 1% here).

A comparison of the mean thicknesses predicted by the model with those of the experiments in Sec. II is displayed in Fig. 4(a). The data show how exchange of momentum between air and liquid flow is qualitatively captured by the model, though the model consistently overpredicts the film thickness. We also track the speed of the waves that develop in each simulation, and their mean wavelength. A comparison of the speeds and wavelengths in our model simulations with the results from Sec. II can be seen in Figs. 5(a) and 5(b).

We note that as the effective viscosity in the turbulent closure we used assumes a smooth wall, its value may be too low for experiments with a wavy air-liquid interface. We briefly examine how increasing the viscosity may improve the quantitative agreement between the model and experiments. Data from a previous study [23] suggest using a phenomenologically modified effective viscosity

$$\mu_{\text{eff}}^{(g)} = \left(\frac{\mu^{(l)}}{\mu^{(g)}}\right)^{1/5} 0.0791 \frac{(\text{Re}_D)^{3/4}\mu^{(g)}}{16}. \qquad (23)$$

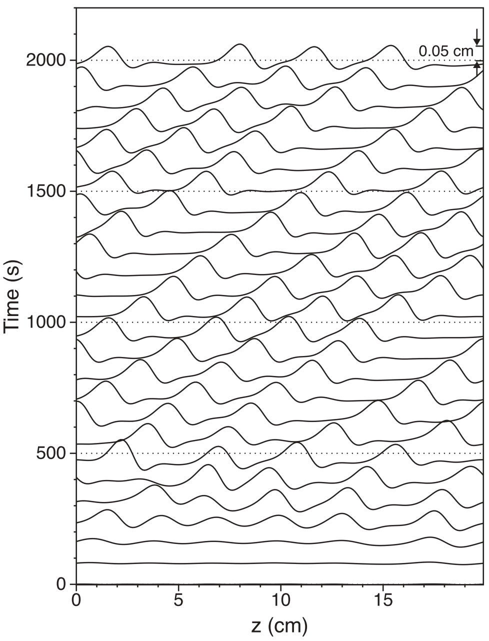

FIG. 9. Same as Fig. 8 but with $S \approx 2.45$ and $\Delta t = 80$ s.

We remark that the additional scaling by the ratio of viscosities of the fluids lies outside the turbulent closure model for the airflow and is suggested purely by phenomenological comparison with a subset of the experimental data; all other points in the data set also closely follow this law. Using this modified viscosity the simulations are repeated and the model is found to predict thicknesses and liquid speeds much closer to those seen in the experiments. Results are shown for $\mu^{(l)} = 129$ P in Fig. 10 (cf. Fig. 4; similar improvements are found for $\mu^{(l)} = 600$ P). We note here that while this agreement shows the model can offer predictive insight, the improvement in mean thickness may be offset by less accurate quantification of other properties, specifically mass transport by the waves. A discussion of these quantitative capabilities of the model is taken up at the end of this section and in Sec. VI.

Once the evolution has settled into a quasi-steady state, we look for a traveling wave solution which satisfies the ordinary differential equation

$$[-c + S_1 f_1(R;a) + S_2(a) f_2(R;a)]R' + \frac{S_3}{R}\frac{d}{dZ}[f_3(R;a)(R' + R^2 R''')] = 0, \qquad (24)$$

where we have moved to a frame of reference moving with the wave, i.e., the independent variable is $Z = z - ct$. With the quasi-steady PDE solution as the initial guess, we use a collocation method two-point boundary value problem solver to refine the solution; conservation of volume is monitored as before.

To explore mass transport mechanisms of the annular fluid on the basis of streamline topology, we reconstruct the stream function defined by the velocity field:

$$u = -\partial_z \Psi, \quad w - c = \frac{1}{r}\partial_r (r\Psi). \qquad (25)$$

The radial velocity u may be found by using w (calculated for the previous section) and the continuity equation (5). By

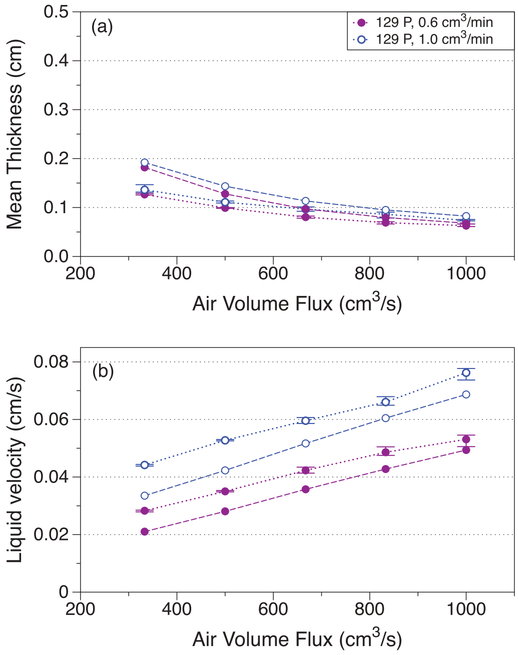

FIG. 10. (Color online) (a) Comparison of mean thickness predicted by the model with modified effective viscosity (dashed lines) with those of the experiments (dotted lines) in Sec. II with $\mu^{(l)} =$ 129 P. (b) Mean liquid cross-sectional average velocities calculated using data in panel (a).

integrating (25) the stream function is given by

$$\Psi = \left[-\frac{S_1}{R^4} + \frac{S_2}{2} + \frac{4S_3}{R^2}(R_z + R^2 R_{zzz})\right]\left[\frac{1}{4r}(a^2 - r^2)^2\right] - [S_2R^2 + 8S_3(R_z + R^2R_{zzz})] \times \left\{\frac{1}{4r}[a^2 - r^2 + 2r^2\ln(r/a)]\right\}. \qquad (26)$$

We are now in a position to plot streamlines within the annular fluid for a variety of parameter values. We want to compare flows with different parameters, e.g., capillary number, at a fixed liquid volume flux. In order to hold this mean liquid volume flux constant as the capillary number is changed, the mean film thickness is adjusted as needed.

Two examples with identical liquid flux but differing capillary number and film thickness are shown in Figs. 11 and 12. (We remark that the parameter values for these waves do not correspond to those in the experiment and these model results only show qualitative agreement with the experimental data.) The fluid for the wave in Fig. 11(a) flows along open streamlines only, while the wave in Fig. 12(a) displays a region of closed streamlines under the wave crest. This closed streamline pattern is a trapped core, a liquid vortex ring, that rotates while translating at wave speeds. Taking axisymmetry into account, there is a separatrix sheet between the train of trapped cores and the wetting layer. Closed streamlines were also identified in the water-oil flow regime of Kerchman [2]. We remark that *all* traveling wave solutions for this model (21) exhibit a trapped core: This is an artifact of eliminating the cylindrical geometry from (13), thus removing the model's ability to conserve mass. The more refined model (13) restores the possibility of traveling wave solutions without trapped cores.

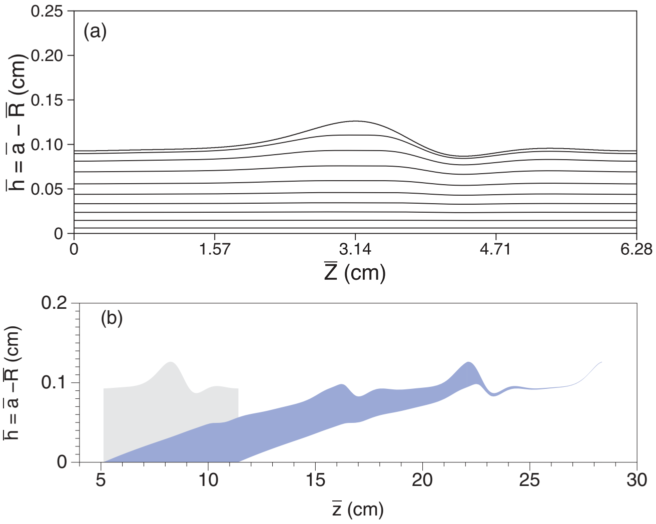

FIG. 11. (Color online) (a) Streamlines in the annular fluid phase for a traveling wave solution of model (13) with parameters $F = 3.39$, $S = 1.5$, $\bar{a} = 0.5$ cm, $a = 1.25$, $Q^{(l)} = 3.2 \times 10^{-4}$cm/s. (b) Evolution of one wavelength of fluid during the interval $t =$ (0,5000)s.

Figures 11(b) and 12(b) show the evolution of the fluid film in each flow. The lightly shaded area represents a region of the fluid film along one wavelength at an initial time. Particle trajectories were calculated for particles lying on the boundary of this region, and the location of the fluid area after a fixed elapsed time is shown by the darker shaded region. Note that the very fastest particles in the shear wave flow [Fig. 11(b)] have traveled almost exactly the same axial distance as the particles in the trapped core in Fig. 12(b). However, any parcel of fluid in the shear wave regime is continuously thinning while stretching in the axial direction, so that the percentage

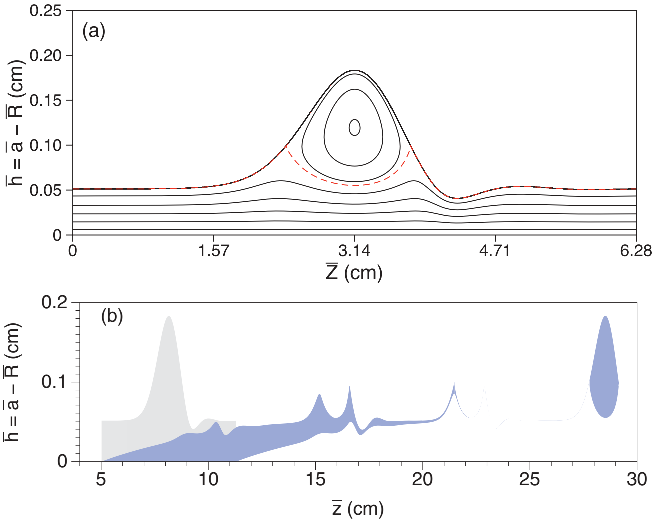

FIG. 12. (Color online) Same as Fig. 11 but with $F = 4.36$, $S =$ 8.96, $\bar{a} = 0.5$ cm, $a = 1.17$, $Q^{(l)} = 3.2 \times 10^{-4}$cm/s. The dashed (red) streamline in (a) is close to a separating streamline.

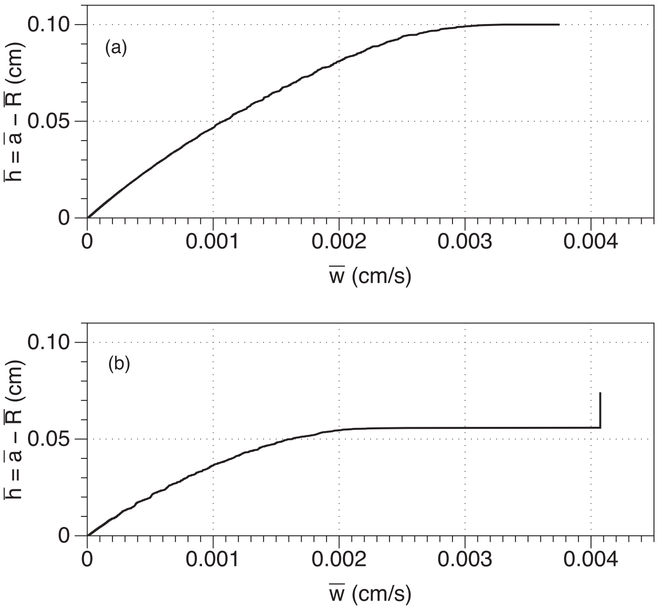

FIG. 13. The flat-interface shear velocity profile equivalent to that of (a) Fig. 11(a) and (b) Fig. 12(a).

of the fluid parcels reaching a certain location at a given time is much smaller than its trapped core counterpart, where the whole core keeps its volume and shape intact.

This point is further illustrated in Figs. 13 and 14. Here a sampling of fluid parcels throughout the fluid domain in Figs. 11 and 12 were tracked over time, and their mean velocities with respect to time calculated. These mean velocities were then sorted, giving an equivalent shear velocity profile, i.e., a flat-interface shear flow with the plotted axial velocity profiles would be equivalent to the two traveling wave flows. In Fig. 13(b) note the significant portion of fluid, corresponding to trapped cores, moving at a uniform speed faster than any particle for the shear wave case in Fig. 13(a). Figure 14 displays the corresponding distribution as a histogram for the velocities shown in Fig. 13. Note the presence of a trapped core is clearly revealed by the spike in velocity at exactly the speed of the wave in Fig. 14(b), while no fluid parcels travel at the speed of the wave in Fig. 14(a). The spike corresponds to the significant volume of fluid in the trapped core in Fig. 12.

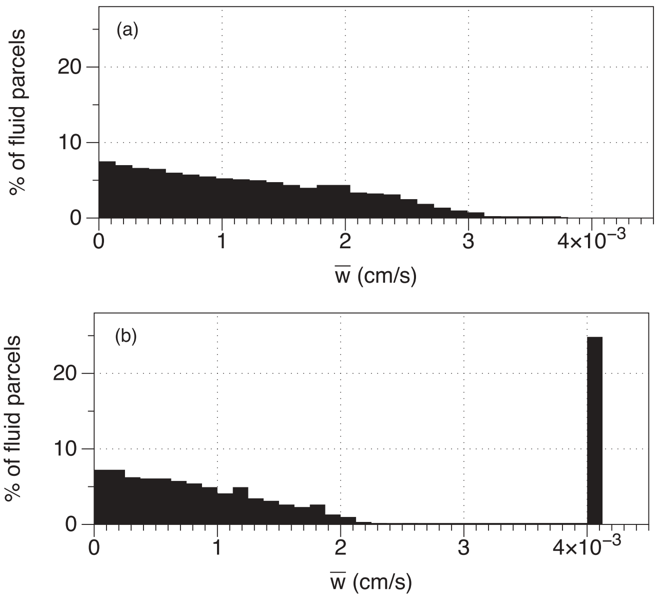

FIG. 14. Distribution of velocities used to construct the shear profiles depicted in Fig. 13.

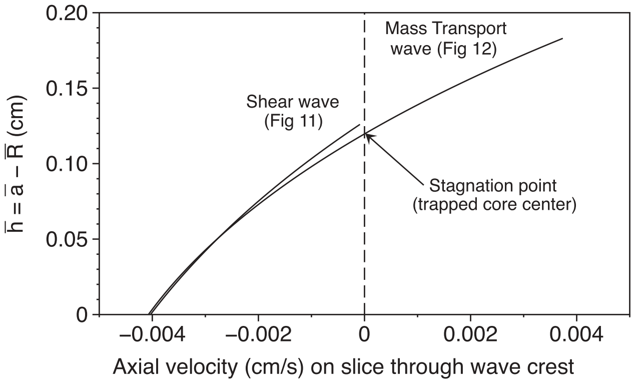

FIG. 15. Liquid parcel axial velocities (measured in the traveling wave reference frame) along radial slices through the wave crest of Figs. 11(a) and 12(a).

In order to be certain that waves like Fig. 11(a) do not trap a core which is masked by under-resolution in the streamlines, we plot the axial velocity of the fluid (relative to the wave velocity) as a function of *r* along one radial slice through the wave crest of Figs. 11(a) and 12(a). Figure 15 shows the velocity profile corresponding to Figs. 11(a) and 12(a). For the shear wave in Fig. 11(a), the velocity is negative throughout the fluid layer, indicating that a trapped core cannot exist. For the mass transport wave in Fig. 12(a), the velocity changes signs at the stagnation point, clearly indicating the existence of a trapped core. This change of streamline pattern with parameters is typical of dynamical systems's bifurcations whereby hyperbolic fixed points coalesce with their center counterparts, leading to the removal of connecting heteroclinic trajectories (see, e.g., Ref. [28] for a discussion in a context appropriate to viscous fluids). Note that the shear wave's velocity profile close to the interface very nearly approaches the speed of the wave, so that a very small change in capillary number would result in the formation of a trapped core.

Figure 16 shows the location of each regime in parameter space for a sample fixed thickness and wavelength. As *S* or *F* decreases, the amplitude of a traveling wave solution decreases, and solutions trap a smaller core and eventually none at all. Parameter values corresponding to a sample experiment with various air viscosities, including the modified effective viscosity, are shown; parameters corresponding to Fig. 11 are also shown. For this experiment (and all experiments conducted) the model predicts waves which are well inside the shear wave regime. It should also be noted that for large values of *F*, larger than those shown here, gravity dominates effects from the airflow and upward-moving traveling wave solutions give way to downward-moving solutions. These solutions exhibit the same type of bifurcation, where some combinations of parameter values result in mass transport waves while others result in shear waves. As these waves are

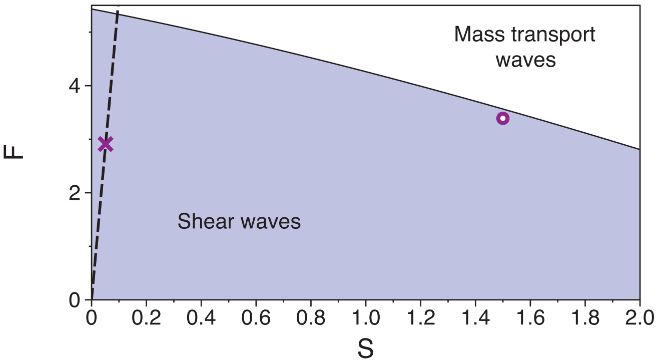

FIG. 16. (Color online) Mass transport and shear wave regimes for traveling wave solutions with fixed $\bar{a} = 0.5$ cm, $a = 1.25$, and $\bar{\lambda} = 2\pi$ cm. Values of S and F, which correspond to the experimental parameters $\mu^{(l)} = 129\,\mathrm{P}$, $Q^{(l)} = 0.6\,\mathrm{cm}^3/\mathrm{min}$, $Q^{(g)} = 667\,\mathrm{cm}^3/\mathrm{s}$, and various air viscosities are indicated by the dashed line; the modified effective viscosity is indicated by the purple "x." Parameter values corresponding to Fig. 11 are indicated by the purple "o."

outside the scope of the present experiments, we leave this topic for future study.

The wave profiles displayed in Figs. 11(a) and 12(a) each exhibit a slight depression in front of the wave crest (traveling left to right) regardless of the presence or absence of closed streamlines. This depression is also seen in the thin-film model [2]. Indeed, this fore-aft asymmetry in the wave profiles is also observed in simulations of propagating liquid plugs [22]. It is interesting to speculate that some features of the free surface and liquid flow pattern in Ref. [22] survive through many orders of magnitude scalings of surface shear stress and Reynolds number of the gas phase.

We remark that, while the model captures the qualitative dynamics seen in the experiment, more work remains to be done to achieve a quantitative comparison between wave parameters generated by the model and those observed in the experiment. For instance, the experiments in Sec. V show evidence of trapped core waves (i.e., waves with closed streamlines as in Fig. 12) in parameter regimes that lie outside of those where this class of waves can be found as model solutions. The modified phenomenological effective viscosity (23) improves thickness predictions, at the expense of traveling wave properties, by generally leading to smaller amplitudes and hence open streamlines. This can be due to a number of reasons: first, the closure assumption for turbulence of the air flow we have used is fairly simple and may be insufficient for modeling the stress at the liquid-air interface. Next, the boundary conditions used in the model are periodic unlike those of the experiment. Modeling of the inflow and outflow boundary conditions within the asymptotic approximations brings up a number of mathematical technicalities (mainly due to the higher order derivatives in the PDE) that lie outside the scope of this experimental investigation.

V. MASS TRANSPORT EXPERIMENTS

We turn now to an experimental verification of mass transport by trapped-core ring waves. While Fig. 2 certainly suggests discrete advances of the wetting front when waves arrive, the data are insufficient to discriminate mass waves from shear waves. To do so we construct a variation of the previous experiment, this time with two glass tubes, two chambers, and two silicone oils, one dyed blue and the other left clear. Other than color, both oils are identical in viscosity and density. As before each chamber is filled with liquid at a constant volume flux, and air is forced upward through each tube.

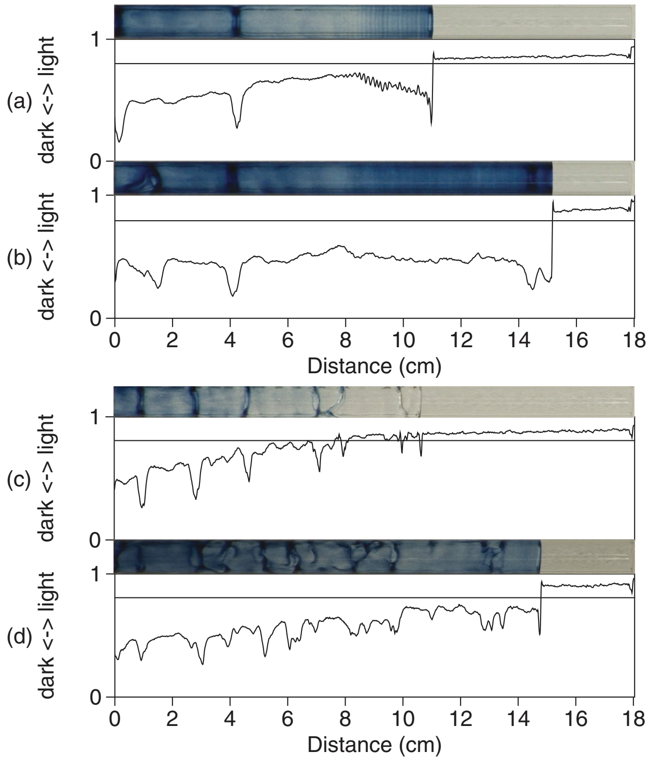

FIG. 17. (Color online) Snapshots of a tube coated partway with clear oil, then coated with blue dyed oil. Companion plots register the color intensity along an average slice. Above (a), (b): Gas volume flux = 500 cm^3/s. (a) $t = 183.5$ s, (b) $t = 348.5$ s after dyed coating begins. Below (c), (d): Gas volume flux = 1000 cm^3/s. (c) $t = 113$ s, (d) $t = 217$ s after dyed coating begins. The horizontal line represents the color intensity of a tube coated only with clear oil.

Dual experiments progress until the wetting front reaches a predetermined height in both tubes. The tubes are then quickly swapped, so that the tube partially wetted with a clear oil layer is thereafter supplied with dyed oil, and vice versa. In the shear wave scenario, dyed oil introduced into the tube will remain near the bottom of the tube, while clear oil will continue to occupy the advancing front. In the mass waves scenario, dyed oil will be transported, with some mixing, over the clear wetting layer to the advancing front. The result of the mass transport will be to saturate both the bottom of the tube and the wetting front with dye, while leaving clearer oil in between.

Experiments at relatively low airflow rate ($Q^{(l)} = 500\,\mathrm{cm}^3/\mathrm{s}$) match the latter, mass transport, expectation. They reveal that some dyed oil introduced into the clear-coated tube remains in the lower portion of the coating [see Figs. 17(a)–17(b)] while the rest of it is transported all the way to the wetting front. Thus we find that a significant portion of dyed oil in the ring wave flows relative to the clear wetting layer.

The rest of it mixes with the wetting layer as it travels. At some later time, the top and bottom tube sections consist mostly of dyed oil, while the middle consists mostly of clear oil. In a companion experiment, this time with clear oil pumped over a blue layer, the dynamics appear to be the same.

Figure 17 shows snapshots of a tube that was partially coated with clear oil, then coated with dyed oil at two different airflow rates. The color intensity of the snapshots is plotted below each with low intensity indicating darker blue. To generate these plots, the intensity was averaged along nine parallel slicing lines connecting one end of the tube to the other. The horizontal line represents the color intensity of the tube coated only with clear oil.

In Figs. 17(a)–17(b) the bottom (left) of the tube has fallen well below this baseline value indicating the clear oil has been "pushed" further up the tube and replaced by the dyed oil. The top (right) of the tube has also fallen well below this baseline value indicating the dyed oil has been transported via waves past the clear oil. The waves are the dark bands in the snapshots, and they advance up the tube, here from left to right. A rise in the middle of the intensity plots indicates that there is a greater concentration of clear oil in the annular layer at the center of the tube; blue mass waves have glided over the layer and dumped blue oil at the front. This phenomenon matches what is seen in traveling wave solutions of the model (13); cf. Fig. 12(b).

We underscore that the strength of this mass transport phenomenon depends on the experimental parameters. Figure 17(c)–17(d) shows the same experiment described above, this time completed with higher airspeed. Note that unlike Figs. 17(a)–17(b) the top (right) of the tube does not approach the intensity of the blue oil. The waves are not transporting blue oil to the top as efficiently as they did at lower airspeed. This can be attributed to two effects. With less coherent wave motion, and partial loss of axial symmetry occurring at higher airspeeds, leakage and mixing of the trapped wave cores is increased. Moreover, as the model suggests, the smaller amplitude waves occurring at higher airspeeds imply smaller trapped cores or even their absence, i.e., streamlines open in the manner depicted by Fig. 11(a). Both effects would make mass transport by waves less efficient. (The slight offset of the intensity for a dry portion of the tube noticeable from Figs. 17(a)–17(d) can be accounted by the camera aperture adjusting for the darker portion of the tube.)

It is also interesting to note the presence of very thin bands of dyed oil near the wetting front in Fig. 17(c). Each band appears to correspond to a single wave that has dumped its mass (containing dyed oil) at the wetting front, advancing the front up the tube. The bands then provide a record of the location of successive breaking waves at the wetting front. [Over time, as the dye concentration at the front increases, these bands become less distinguishable; e.g., no bands are visible in Fig. 17(b).]

Figure 18 presents the time history counterpart of the spatial snapshots from the experiment in Fig. 17. We fix two locations along the tube for which the arrival time of the wetting front is the same and record one-pixel-wide cross-sectional images as time progresses at 30 fps. The montage of these images thus gives the evolution of blue dye concentration at each fixed location in time. In Fig. 18(a) the blue oil appears coincidentally with the liquid wetting front. Here mass waves have brought blue oil quickly to the front, dumping the highly concentrated dye. By contrast, Fig. 18(b) shows that a shear-dominated flow pulls blue color up the tube more slowly. The dark band in this montage is not blue; it is merely the dark refractive cast of the slow-moving front. Thus the fastest way for newly injected particles to move up a wetting tube is to catch a ride on the next available mass transport wave.

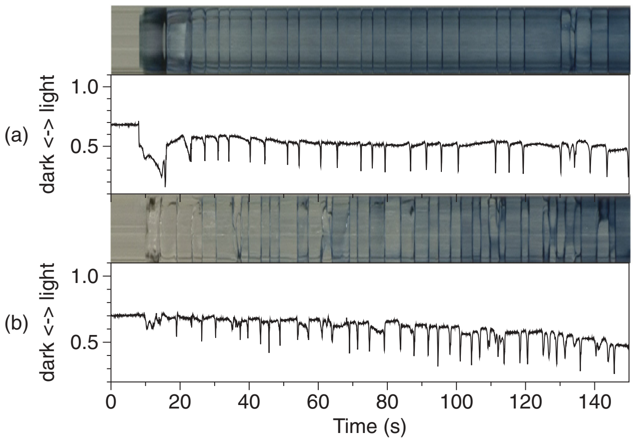

FIG. 18. (Color online) Evolution of a vertical slice of pixels from the same tube as in Fig. 17. Companion plots once again register the color intensity along an average horizontal slice. (a) Gas volume flux = 500 cm^3/s, location = 8.9 cm from bottom of tube. (b) Gas volume flux = 1000 cm^3/s, location = 10.6 cm from bottom of tube. Blue color increases abruptly with the liquid front in panel (a), in contrast with the gradual increase in panel (b).

In lung airways, the mucus layer interfaces with a less viscous lining called the periciliary layer (PCL). The dyed-clear oil experiment was repeated with the prewetted clear oil having a lower viscosity in order to see how this viscosity contrast affects the mass transport waves. As before the tube was partially coated with the clear (less viscous) oil, then coated with the dyed (more viscous) oil. The ring waves of dyed oil are less stable gliding on this less viscous layer; some breakup and asymmetry of the waves were observed. Nevertheless, the same phenomenon of waves carrying dyed oil to the wetting front persists.

The mass transport features identified above persist over a large experimental and theoretical range. As described above, our wave-tracking experiments were conducted with various air flow rates (333, 500, 667, 833, 1000, 1167 cm^3/s), liquid flow rates (0.6, 1.0 cm^3/min), and liquid viscosity (129, 600 P). (An example of less regular wave activity is shown in Fig. 3.)

VI. DISCUSSION

We have identified both theoretically and experimentally a mass transport mechanism for a wide range of core-annular flow regimes where the annular-to-core viscosity ratio spans many orders of magnitude. The mechanism is due to vortex ring waves of the annular fluid spawned by air-driven interfacial instabilities and inflow irregularities which amplify as they propagate upward. The strength of this mass transport mechanism is experimentally and theoretically tunable, e.g., by varying airflow rate. While the long-wave asymptotic model derived here qualitatively captures many of the features seen in the experiments, achieving quantitative predictive agreement requires further work. Nonetheless, the present study establishes the groundwork for future improvements at the modeling level, and preliminary results in ongoing studies suggest that one area to focus attention on for improvements would be that of careful estimates of the interfacial stress created by the (turbulent) gas flow.

From an application viewpoint, while the conditions under which the experiments were performed clearly do not match those found in the lungs and airways (e.g., rigid glass tube, unidirectional airflow, Newtonian fluids), the fundamental aspects of this mass transport mechanism, in large lung airways, are potentially relevant and can even be important for optimizing therapeutic strategies. More study of this phenomenon under conditions closer to those found in airways is needed, some of which is currently underway.

ACKNOWLEDGMENTS

This project derives from the Virtual Lung Project at UNC. We thank Zane Beckwith, Eugene Dumitrescu, Michael Jenkinson, Jeeho Kim, Matthew Lynley, John Mellnik, Shreyas Tikare, and Leandra Vicci for experimental contributions. R.C. and R.O. are also grateful to K. Zumbrun for helpful discussions on the structure of the mathematical model. This research was supported by NSF DMS-0509423, DMS-0908423, DMS-1009750, RTG DMS-0943851, and NIEHS 534197-3411.

---

[1] D. D. Joseph and Y. Renardy, *Fundamentals of Two-Fluid Dynamics, Part 2: Lubricated Transport, Drops, and Miscible Liquids* (Springer, New York, 1993).

[2] V. I. Kerchman, J. Fluid Mech. **290**, 131 (1995).

[3] P. S. Hammond, J. Fluid Mech. **137**, 363 (1983).

[4] C. Kouris and J. Tsamopoulos, Phys. Fluids **13**, 841 (2001).

[5] C. Kouris and J. Tsamopoulos, Phys. Fluids **14**, 1011 (2002).

[6] L. W. Schwartz, H. M. Princen, and A. D. Kiss, J. Fluid Mech. **172**, 259 (1986).

[7] D. T. Papageorgiou, C. Maldarelli, and D. S. Rumschitzki, Phys. Fluids A **2**, 340 (1990).

[8] A. L. Frenkel, Europhys. Lett. **18**, 583 (1992).

[9] C. Hickox, Phys. Fluids **14**, 251 (1971).

[10] R. W. Aul and W. L. Olbricht, J. Fluid Mech. **215**, 585 (1990).

[11] H. H. Hu and D. D. Joseph, J. Fluid Mech. **205**, 359 (1989).

[12] V. I. Kerchman and A. L. Frenkel, Theor. Comput. Fluid Dyn. **6**, 235 (1994).

[13] D. Joseph, M. Renardy, and Y. Renardy, J. Fluid Mech. **141**, 309 (1984).

[14] M. Johnson *et al.*, J. Fluid Mech. **233**, 141 (1991).

[15] D. Halpern and J. B. Grotberg, J. Fluid Mech. **244**, 615 (1992).

[16] R. Levy, E. Peterson, M. Shearer, and T. Witelski, in *Proc. 12th International Conference on Hyperbolic Problems, College Park, Maryland*, edited by E. Tadmor, J. Liu, and A. Tzavaras (AMS, Providence, RI, 2009), p. 855.

[17] R. Levy, M. Shearer, and T. P. Witelski, Eur. J. Appl. Math. **18**, 679 (2007).

[18] S. W. Clarke, J. G. Jones, and D. R. Oliver, J. Appl. Phys. **29**, 464 (1970).

[19] C. S. Kim *et al.*, J. Appl. Phys. **60**, 901 (1986).

[20] C. S. Kim *et al.*, J. Appl. Phys. **60**, 908 (1986).

[21] C. S. Kim, A. J. Iglesias, and M. A. Sackner, J. Appl. Phys. **62**, 959 (1987).

[22] S. Ubal *et al.*, Ind. Eng. Chem. Res. **47**, 6307 (2008).

[23] R. Camassa and L. Lee, in *Advances in Engineering Mechanics: Reflections and Outlooks*, edited by A. Chwang, M. Teng, and D. Valentine (World Scientific, Singapore, 2006), p. 222.

[24] A. Oron, S. H. Davis, and S. G. Bankoff, Rev. Mod. Phys. **69**, 931 (1997).

[25] F. M. White, *Viscous Fluid Flow* (McGraw-Hill, New York, 1991).

[26] R. W. Aul, Ph.D. thesis, Cornell University, Ithaca, NY, 1989.

[27] M. Johnson, P. Noble, L. M. Rodrigues, and K. Zumbrun, arXiv:1202.6402v1.

[28] T. Ma and S. Wang, Nonlin. Anal. **1**, 467 (2001).